





# Adaptive Local Flaw Detection Based on Magnetic Flux Leakage Images With a Noise Distortion Effect for Steel Wire Ropes

Feiyang Pan , Zhiliang Liu , *Member, IEEE*, Liyuan Ren , and Mingjian Zuo , *Senior Member, IEEE*

**Abstract**—A steel wire rope (SWR) is widely used in industrial scenarios because of its high strength and toughness. To avoid accidents that local flaws (LFs) can cause, SWRs should be inspected regularly. Magnetic flux leakage (MFL) image detection, which is a common SWR inspection method, is inevitably influenced by shaking noise and strand noise. Although noise-reduction methods for these two types of noise have been proposed, the phenomenon of noise distortion has not received enough attention. In this article, we investigate the noise distortion phenomenon on the MFL image and finds that the distorted noise severely affects the performance of existing noise-feature-oriented denoising methods. To solve this problem, we adopt a target-feature-oriented (TFO) denoising method. Specifically, the removal of noise is avoided; instead, an LF-enhancement-based denoising process is proposed. Moreover, to localize LFs in denoised images, a three-stage adaptive localization method mainly based on disjoint region analysis is proposed. The experimental results show that the proposed TFO denoising method significantly improves the denoising performance for images that distorted noise influences. In addition, the proposed adaptive localization method improves the intelligence of the localization process and has better localization performance for images with distorted noise.

**Index Terms**—Distorted noise, image processing, local flaw (LF) detection, magnetic flux leakage (MFL), steel wire rope (SWR).

## I. INTRODUCTION

STEEL wire rope (SWR) is a helical steel wire bundle twisted by several spiral strands of steel rope made of high-strength steel [1]. In many large industrial applications, SWR is often used as a key load-bearing component for fixing, lifting, and pulling large weights [2]. Throughout the use process, the SWR's surface is inevitably affected by collisions and scrapes when contacting other equipment [3], resulting in various local flaws (LFs). LFs on the surface can further lead to the entire SWR breaking, thus posing a serious threat to system safety [4]. Therefore, periodical inspection of the SWR and replacing abnormal SWRs according to the inspection results are of great practical importance in industrial applications.

Nondestructive testing (NDT) is often used in diagnosing SWRs because it avoids irreversible damage to the SWR during the diagnosis process. The NDT can be implemented through manual detection [1], visible image detection [5], [6], [7], [8], [9], ultrasonic wave detection [10], and electromagnetic detection [11], [12], [13], [14], [15]. The magnetic flux leakage (MFL) detection is a type of electromagnetic detection method in which the magnetic sensor detects the abnormal magnetic leakage field LFs generate on the magnetized SWRs. Due to its efficiency and stability, the MFL detection method is now one of the most promising SWR detection methods. The MFL detection method usually has two common acquisition modes for inspecting the SWR: single-channel and multichannel data acquisition modes [16]. When using single-channel equipment, the LF signal can be detected by identifying the impulse-shaped signal after proper signal processing. However, according to the existing studies, the single-channel detection methods often have higher false detection rates and miss detection rates under the influence of noise (especially shaking noise) [18]. Therefore, the multichannel equipment, which can provide 2-D spatial information, is more widely used in SWR detection.

According to previous studies, the MFL diagnosis process often contains two critical steps: denoising and localization [17], [18], [19], [20], [21]. The denoising process reduces the influence of MFL signal noise and increases the signal-to-noise

Manuscript received 27 September 2022; revised 14 January 2023, 22 February 2023, and 29 March 2023; accepted 24 April 2023. Date of publication 10 May 2023; date of current version 27 October 2023. This work was supported in part by the National Key Research and Development Program of China under Grant 2018YFB1702400 and in part by the National Natural Science Foundation of China under Grant 61833002. (Corresponding author: Zhiliang Liu.)

Feiyang Pan is with the Glasgow College, University of Electronic Science and Technology of China, Chengdu 611731, China (e-mail: panfeiyang624@mail.uestc.edu.cn).

Zhiliang Liu is with the School of Mechanical and Electrical Engineering, University of Electronic Science and Technology of China, Chengdu 611731, China (e-mail: zhiliang\_liu@uestc.edu.cn).

Liyuan Ren is with the Glasgow College, University of Electronic Science and Technology of China, Chengdu 611731, China (e-mail: l.ren-1@student.tudelft.nl).

Mingjian Zuo is with the Qingdao International Academician Park Research Institute, Qingdao 266041, China, and also with the School of Mechanical and Electrical Engineering, University of Electronic Science and Technology of China, Chengdu 611731, China (e-mail: zuo.mingjian@mingserve.com).

Color versions of one or more figures in this article are available at <https://doi.org/10.1109/TIE.2023.3273250>.

Digital Object Identifier 10.1109/TIE.2023.3273250

ratio (SNR), which is the key step in increasing inspection accuracy. The denoising method mainly focuses on removing the strand noise and the shaking noise [21]. Essentially, strand noise is the MFL signal fluctuation that the uneven and periodical surface of SWR causes. Shaking noise is the sudden change of the MFL signal that the shaking of the SWR and the detector cause.

The existing denoising methods are mostly noise-feature-oriented (NFO) methods. This type of method depends on noise features that are stable and different from LF features. Various NFO denoising methods were developed by considering noise features from different perspectives. For the frequency-feature-based method, notch filter [22] and the compressed sensing wavelet filtering method [19] can reduce strand noise. For the spatial features-based method, Zhou and Liu [17] proposed a denoising method based on multichannel spatial information of the strand noise and shaking noise. Ren et al. [18] improved the elimination of shaking noise by using the circular median filter on channel direction. Moreover, the 2-D noise features-based denoising methods are also effective. The noise's texture [23] and morphological features [21] can also suppress noise according to existing studies. Regarding the localization process, it works on the denoised MFL signal or image, which is often assumed to have a high SNR, to determine the existence and the locations of LFs. The constant threshold method is commonly used in localizing LFs [17], [18]. Canny edge detection [11] and mapped binary data method [19] can also localize the LFs.

The abovementioned studies have proposed many meaningful methods to reduce the noise and localize LFs. However, most of these NFO methods assume stable and consistent noise features. When noise is distorted, which is often unavoidable in practice, the existing NFO methods' performance can be greatly affected. There are two new challenges the noise distortion phenomenon causes.

- 1) The existing NFO denoising methods assume that both shaking noise and strand noise have constant and specific features under all detection conditions. However, in engineering practice, these two types of noise are vulnerable to distortion, which various and unpredictable abnormal working conditions cause. Consequently, the existing NFO method may suffer.
- 2) The existing localization methods rely on high SNR results from the denoising process. If there are residual distorted noises after the denoising process, they can be easily recognized as false positives. However, if the sensitivity of recognition is decreased to reduce the false positive rate, nonobvious LFs with low signal magnitudes can be missed.

At this moment, no other groups have focused on the distorted noise challenges mentioned above. To overcome these challenges, in this article, we propose a novel SWR diagnosis method based on MFL image processing. This article's main contributions can be summarized as follows.

- 1) We analyze the noise distortion phenomenon on MFL images and explore its influence on existing NFO denoising methods.

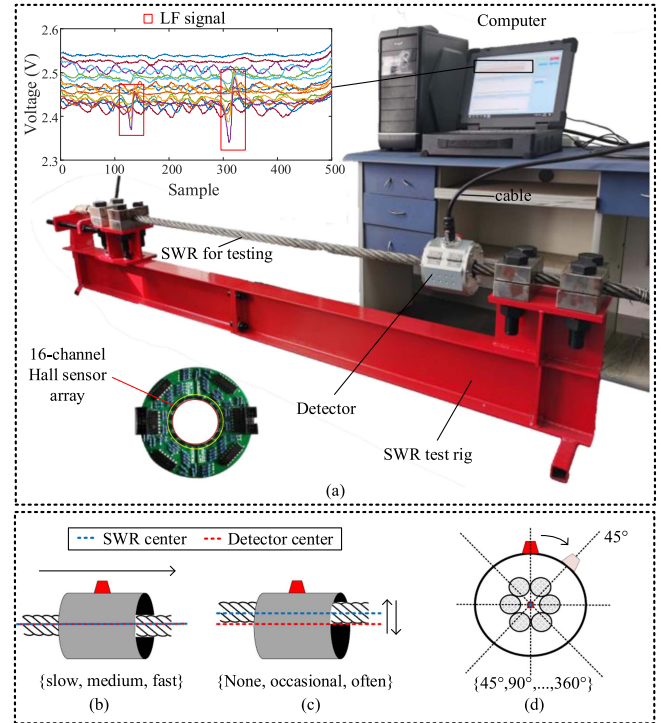


Fig. 1. MFL data acquisition system and schematic of different detection scenarios. (a) MFL data acquisition system. Scenarios of (b) different detector moving speed, (c) different SWR jitter frequency, and (d) different detector orientation.

- 2) We propose a novel denoising method to improve SNR under the noise distortion phenomenon. The proposed method adopts a target-feature-oriented (TFO) principle rather than NFO principle.
- 3) We propose a three-stage adaptive localization method to detect LFs under the influence of a residual distorted noise signal. This adaptiveness improves the accuracy of the LF detection.

The rest of this article is organized as follows. First, the apparatus and the process of MFL data acquisition are described in Section II. The noise distortion phenomenon and its influence are explored and analyzed in Section III. After that, details about MFL image generation, LF enhancement, and the adaptive localization method are provided in Section IV. Then, a case study is explored in Section V, and the performance comparison is provided in Section VI. Finally, Section VII concludes the article.

## II. MFL DATA ACQUISITION

This section provides information about the SWR test rig, the MFL data acquisition system, and how the experiments are conducted.

The entire system is developed based on the MFL detection principle Zhou and Liu [17] described, and the schematic is shown in Fig. 1. The tested SWR consists of six strands and two manufactured broken wire LFs. The detector consists of a

16-channel Hall sensor array, which is settled along the circumferential direction [21]. The Hall sensors detect the magnetic signal in the radial direction. The detailed explanations of radial, axial, and circumferential direction and the reason for choosing radial direction can be found in a previous study [17]. The detector is in a twofold structure, which allows it to be folded ON and OFF at any position on the wire rope, while the fixed ring structure can only be attached from the SWR's ends. For moving the detector, our previous work in [17] has already introduced two operating modes that allow the detector to walk on a steel rope. The two operating modes are portable mode and online mode. This article uses the portable mode in all experiments. That is, the experimenter pulls the detector to move along the SWR. The system has been calibrated by gauss meter.

The Hall sensors first transfer the received MFL signals into voltage signals, and then the voltage signals are transmitted to the computer through a data cable. The plot of the 16-channel MFL signal is shown in Fig. 1(a). The Hall sensors sample the magnetic field signal every certain time (equal time sample). It is possible that the samples are converted to axial distance if the moving speed of the detector is given. We can use the following equation to get the corresponding axial distance:

$$d = \frac{vN_s}{F_s} \quad (1)$$

where  $d$  is the moving distance of the detector,  $v$  is the moving speed of the detector,  $N_s$  is the sampling number, and  $F_s$  is the sampling frequency. In our experiments, the speed and the sampling frequency are constants, and thus, the distance is proportional to the sampling number. Therefore, we have not converted the sample to corresponding axial distance since they are equivalent in this article.

To enrich the data's diversity, the experiments are implemented under different acquisition scenarios. The acquisition scenarios are controlled by changing the detector moving speed, SWR jitter frequency, and detector circumferential orientation. In the experiments, the detector is manually controlled. The speed and jitter frequency were both kept in several ranges that corresponded to different inspection scenarios in real applications. By using a narrow range rather than a fixed value, we can further enhance the dataset's diversity.

- 1) As shown in Fig. 1(b), the detector moving speed refers to how fast the detector is moving along the axial direction, which is not always constant under different inspection scenarios. By estimating the time for a single detection process (i.e., sliding the detector from one end of SWR to another), the moving speed can be controlled. In the experiments, the three ranges for the detector moving speed are: slow (0–0.5 m/s), medium (0.5–1 m/s), and fast (1–1.5 m/s).
- 2) As shown in Fig. 1(c), the jitter frequency means the number of times the SWR center moved away from the detector center in 1 s. The jitter frequency is controlled by specifying the number of times of jitter every second. The scenario of no jitter inspection is considered, which corresponds to 0 Hz jitter frequency. The other two ranges

for the jitter frequency are occasional (0–0.5 Hz) and often (0.5–2 Hz).

- 3) As shown in Fig. 1(d), the detector circumferential direction means the sensor array's relative position to the SWR in the circumferential direction, which can often be changed because of the SWR's rotation during real detection. The circumferential direction is simply controlled by rotating the detector around the SWR.

The detector moving speed and SWR jitter frequency has three levels and the detector placement orientation has eight directions. Thus, 72 acquisition conditions ( $3 \times 3 \times 8$ ) can be constructed. In each acquisition condition, the detector is repeatedly moved along the axial direction of the SWR ten times to collect fully the possible inspection data under that condition.

### III. NOISE DISTORTION AND ITS INFLUENCE

In this section, the noise distortion phenomenon is presented and analyzed by considering two distortion examples. The vulnerability of the NFO denoising method and the feasibility of TFO method are also explained.

To distinguish distorted noise from normal noise, reference standards need to be established. The standard strand noise and shaking noise signals are constructed, as shown in Fig. 2(a) and (b) [17], [18]. The ideal strand noise is shown as a group of parallel stripes that have consistent slope and amplitude. The essential property of ideal shaking noise is the signal magnitude difference at two parts of the channel indexes, one with a higher magnitude and the other with a lower magnitude.

After giving standards, the distortion phenomenon can be defined. The standards given above are in the form of feature description. Meaning, if there are differences between the features of observed noise and standard noise features, the observed noise can be seen as distorted.

When there is no distortion noise, using standard noise features can effectively remove the noise. Nevertheless, in practical cases, the noise distortion is often inevitable. Two examples of distorted noise are presented in Fig. 2 with distorted noise marked out. From Fig. 2(c) and (d), clearly, the essential features used to remove noises in NFO methods are influenced because of distortion. Compared to the standard strand noise in Fig. 2(a), strand noises in Fig. 2(c) have obvious difference in magnitudes and slopes in the image's different regions. The strand noise's stripe shape can also be distorted because of noise mixture, as shown in Fig. 2(d). In the case of shaking noise, the step-shaped magnitude difference feature is distorted due to noise mixture, as shown in Fig. 2(d). From this, the distorted noise features can severely affect the performance of the existing NFO denoising methods.

Different from the noise signal, the LF signal, which is the localization target, has a relatively consistent feature. Although the LF's size can influence the LF signal's shape, detector moving speed, lift-off distance, and SWR magnetization intensity, there is still an intrinsic feature for all LF signals. The LF signal always consists of a combination of local adjacent "peak and valley" (the peak refers to the higher magnitude and the valley refers to the lower magnitude) [17]. The LF signals on the



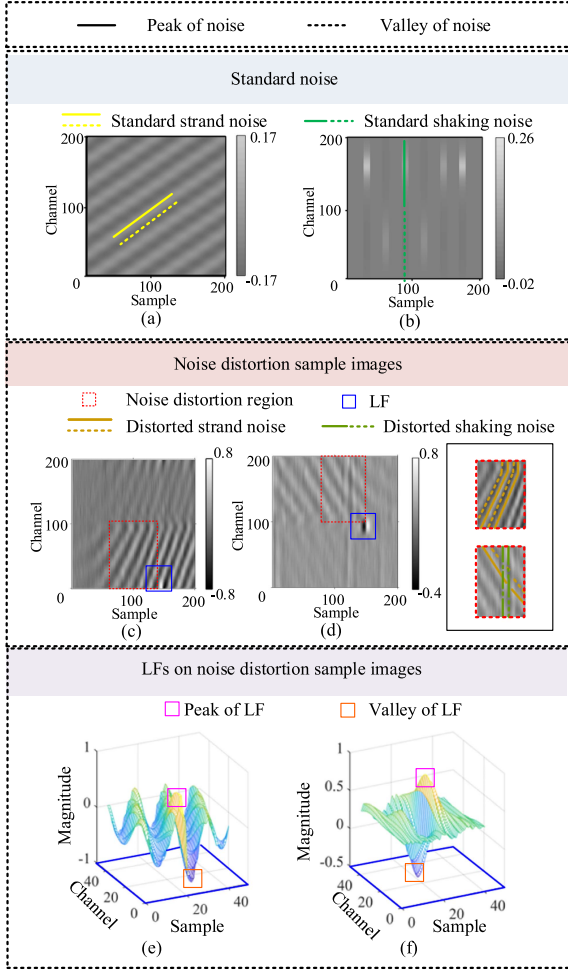


**Fig. 2.** Comparison of standard noise and distorted noise. (a) Simulated standard strand noise image. (b) Simulated standard shaking noise image. Influence of distortion on (c) slope and magnitude features and (d) signal shape features. (e), (f) 3-D view of LF signals in (c) and (d). Solid lines and dashed lines mark the noise shape. The solid line represents the part of noise with high amplitude. The dashed line represents the part of noise with low amplitude.

two-noise distortion example images are extracted and shown in Fig. 2(e) and (f), and as can be seen, both the two LF target signals keep the essential feature (peak and valley) of the typical LF. This finding provides critical evidence for the feasibility of the TFO denoising method proposed in this article.

#### IV. METHODOLOGY

A novel detection method combined with TFO denoising and adaptive localization is described in this section. The steps of the proposed method are illustrated in Fig. 3. The results of the MFL image generation step are MFL image segments, and the results of the LF enhancement step are denoised MFL image segments.

##### A. MFL Image Generation

In our method, the collected MFL signals need to be further processed into image segments for detection. The whole process is illustrated in a flowchart in Fig. 4.

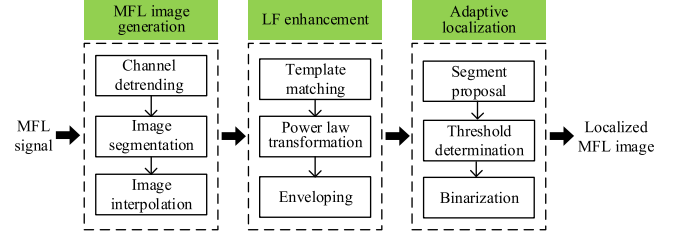


**Fig. 3.** Schematic of the proposed method.

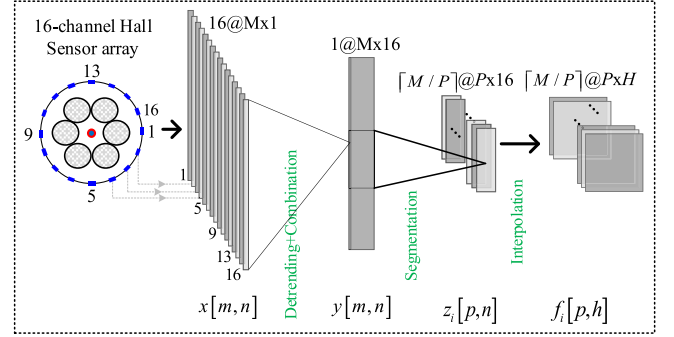


**Fig. 4.** Process of the MFL signal imaging method.

The first step is detrending. In this step, the received 16-channel signal is equalized to the same baseline to highlight the LF signal and eliminate the signal trends' influence [17].

We define the received MFL signal as  $x[m, n]$  for the  $m$ th sample value received in the  $n$ th channel,  $m = 1, 2, \dots, M$  and  $n = 1, 2, \dots, N$ , where  $M$  depends on the times of sampling in each acquisition process, and  $N = 16$  in this article. Accordingly, the process of detrending is defined as

$$b[m, n] = \frac{1}{2L_a} \sum_{k=m-L_a}^{m+L_a-1} x[k, n] \quad (2)$$

where  $b[m, n]$  is the baseline signal,  $2L_a$  is the length of moving average filter, and  $k$  is the internal step of the filter. Then, the detrended signal  $y[m, n]$  can be calculated as

$$y[m, n] = x[m, n] - b[m, n]. \quad (3)$$

After detrending, the 16-channel signal is concatenated into a 16-width image and normalized to the range of  $-1$  to  $1$ . This is because if actual units are still used in the following data processing steps, the units of the data can be changed (e.g., square of the volt) and have no corresponding physical meaning. It is also because only the relative magnitude information of the MFL data is needed for the proposed method. From this, normalization is applied to transfer the detrended data to dimensionless quantities. In this article, figures without captions of actual units (i.e., voltage) use the dimensionless quantities.

Then, the stitched image is segmented into small parts, which are defined as follows:

$$z_i[p, n] = y[p + (i - 1) \times P, n] \quad (4)$$

where  $z_i[p, n]$  is the  $p$ th sample of the  $n$ th channel inside the  $i$ th segment,  $i = 1, 2, \dots, \lceil M/P \rceil$ ,  $p = 1, 2, \dots, P$ , where  $P$  is the length of each segment,  $P = 200$  in this article.

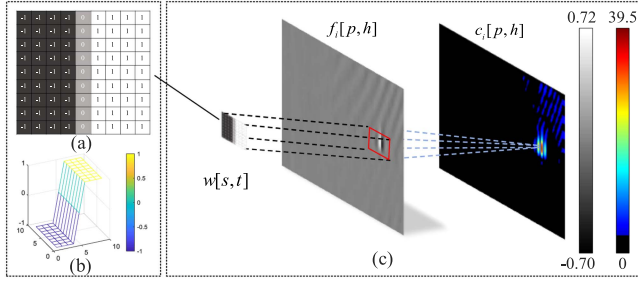


Fig. 5. Process of template matching. (a) Template value map. (b) Template value in 3-D view. (c) Template matching process for a sample MFL image segment.

Finally, the image segments are interpolated to extend the channel direction resolution. According to the empirical knowledge, the spline interpolation method is found to be better than commonly used interpolation methods (i.e., nearest, linear, and cubic). As a result, the spline interpolation method is applied to interpolate image segments  $z_i[p, n]$  to  $f_i[p, h]$  in the channel dimension, where  $h$  is the channel index after interpolation,  $h = 1, 2, \dots, H$ , and we use  $H = 200$  in this article.

## B. Enhancing the LF Signal

The purpose of LF signal enhancement is to improve SNR under distorted noise conditions, which is critical for localization accuracy. The proposed method treats the LF signal as the target and implements the LF signal enhancement method to realize the TFO denoising process.

**1) Template Matching:** The purpose of template matching is to extract the LF signature and represent it by a region containing high template response values.

A template is designed based on the LF signals' spatial properties. According to our analysis in Section III, the LF signal's essential feature is the combination of a peak and a valley. As shown in Fig 2(e) and (f), the magnitude distribution of the LF signal is quite similar to that of the extended Prewitt operator, as shown in Fig 5(b) (i.e., both have a peak and a valley). From the perspective of template matching, the extended Prewitt operator matches the LF signal well [24]. The size of the template is decided based on the average size of the LF signal. Through our prior experiments, we found that a too large-sized template is unsuitable for enhancing the small-sized LF signals, while a too small-sized template is poor at enhancing large-sized LF signals with a separated peak and valley. As a tradeoff, extended Prewitt operator with the size of  $9 \times 9$  is used.

The process of the template matching step in the proposed method includes the convolution and taking the absolute value. The entire process is shown in Fig. 5(c). Absolute value is used to eliminate the influence of LF directionality along the sample direction. The template matching result can be calculated by the following equation:

$$c_i[p, h] = \left| \sum_{s=-a}^a \sum_{t=-b}^b w[s, t] f_i[p+s, h+t] \right| \quad (5)$$

where  $f_i[p, h]$  is the input MFL image,  $w$  refers to the template,  $c_i[p, h]$  refers to the template response result matrix, and  $2a+1$  and  $2b+1$  are the width and height of the template, respectively. In (4), to ensure that the template matching result has the same size as the input image, the zero-padding method is used. To be more detailed, a border of elements all with value 0 is added outside the edge of the image before template matching.

**2) Power Law Transformation:** This step enhances the SNR by using the property of the power law transformation [25].

The template response magnitude of the LF signal is higher than that produced by the distorted noise. The magnitude enhancement degree of the LF signal is much higher than that for distorted noise by using power law transformation. This is because when  $\gamma$  is higher than 1, power law transformation always enhances higher input values to a higher extent.

The power law transformation's effectiveness can be proved. First, the mathematical expression of the SNR calculation formula is defined as

$$\text{SNR} = 20 \log_{10} \left( \frac{S_{\min}}{N_{\max}} \right) \quad (6)$$

where  $S_{\min}$  refers to the minimum amplitude of the LF signal and  $N_{\max}$  refers to the maximum amplitude of the noise. The detailed description of this formula can be found in a previous study [18]. The process of the power law transformation is defined as

$$g_i[p, h] = c_i[p, h]^\gamma \quad (7)$$

where  $\gamma$  refers to the power law transformation coefficient and  $g_i[p, h]$  refers to the result after the power law transformation. SNR before and after power law transformation can be defined as  $\text{SNR}_c$  and  $\text{SNR}_g$ , respectively. SNR after power law transformation can be calculated as

$$\text{SNR}_g = 20 \log_{10} \left[ \frac{(S_{\min} - c)^\gamma}{(N_{\max} - c)^\gamma} \right] = \gamma \text{SNR}_c. \quad (8)$$

From (7), it is obvious that the SNR after power law transformation is multiplied by  $\gamma$ . Thus, when  $\gamma$  is higher than 1, the power law transformation can enhance the SNR defined in (5), regardless of the noise's amplitude and shape.

The power law transformation coefficient is determined by prior experience. The coefficient  $\gamma$  used in this article is 2, which is a reasonable value in our experiments. This value determines the degree of noise suppression. The higher power law transformation coefficient can provide a better noise suppression effect. However, if the coefficient is too large, for image segments with more than one LF signal, lower level LF signals become more difficult to detect in the localization stage (relatively suppressed). From this, the coefficient value is set as 2 as a tradeoff.

By using power law transformation, the SNR is significantly increased, regardless of the noise condition.

**3) Enveloping:** The purpose of enveloping is to represent each LF as a single peak in the power law transformation result.

According to our analysis in Section IV-B, a typical LF signal of broken wire is composed of two extremum regions that are symmetrical and have opposite signs. In the template matching result image, high response values can be observed at locations

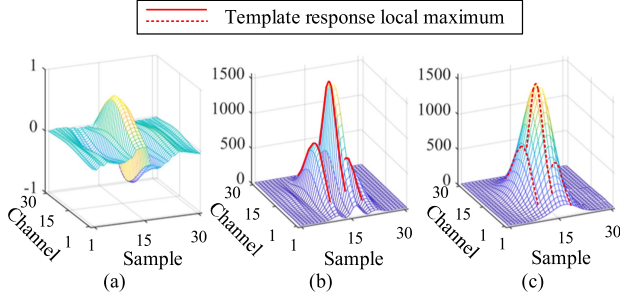


Fig. 6. Enveloping process for the LF signal. (a) Original LF signal. (b) LF signal after template matching and power law transformation. (c) LF signal after taking the envelope.

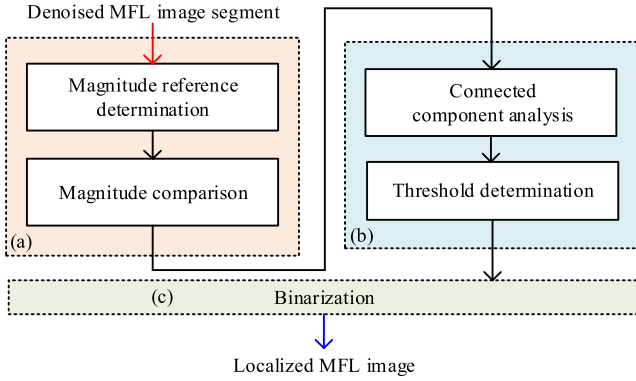


Fig. 7. Flowchart of the three-stage adaptive localization algorithm. (a) Segment proposal stage. (b) Threshold determination stage. (c) Binarization.

where there is a change from one extremum region to another. In addition, the transition region between the nearby region and the extremums can produce a high template response value. From this, in the template response image, LFs are transferred into the form of three stripe peaks, as shown in Fig. 6(b).

The envelope is obtained by finding the local maxima of the pixel values in each channel of the segment and connecting these points by cubic spline interpolation [26]. The process of enveloping is shown in Fig. 6(b) and (c), and we denote enveloping result as  $r_i[p, h]$ .

### C. Adaptive Localization

The localization method used in this article is a three-stage method. The first stage is to find the segments of interest (that contain LF) among all MFL image segments from the same acquisition. The region proposal network in the object detection algorithm inspires this step [27]. The second stage is to implement the segment-based adaptive threshold determination method for all segments of interest. The third stage is binarization. By using the proposed method, LFs can be automatically localized without the requirements for manual threshold setting during the detection process. The schematic of the localization method can be illustrated in Fig. 7.

**1) Segment Proposal Stage:** This stage initially recognizes image segments with LFs.

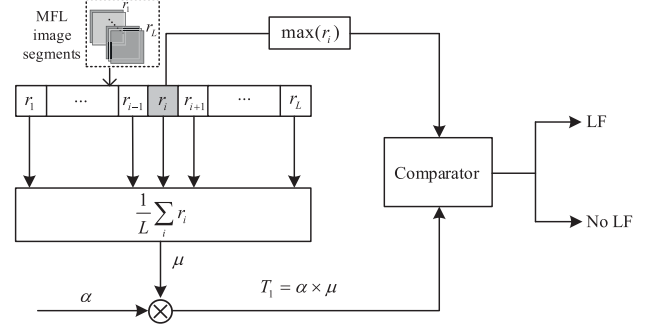


Fig. 8. Schematic of the segment proposal stage.

The method in this stage is inspired by the 1-D constant false alarm rate algorithm used in radar signal processing [28]. Segments with LFs are further processed in the second stage. The schematic of the method in this stage is shown in Fig. 8. A magnitude reference value  $\mu$  is calculated based on the average magnitude of all denoised images under the same detection condition, and the formula is defined as

$$\mu = \frac{1}{L \times P \times H} \sum_i \sum_p \sum_h r_i[p, h] \quad (9)$$

where  $L = \lceil M/P \rceil$ . This value provides a reference for the magnitude information under each detection. By determining a threshold factor  $\alpha$ , a segment proposal adaptive threshold value can be calculated as

$$T_1 = \alpha \times \mu \quad (10)$$

where  $T_1$  is the proposal threshold and the threshold factor  $\alpha$  is set at 7 according to the prior knowledge. The prior knowledge is based on the estimation of magnitude difference between the LF signal and the magnitude reference value. For engineering practice, prior experiments should be done at first. Then, the magnitude reference value  $\mu$  can be calculated based on (8), and the threshold factor can be estimated as a value slightly lower than the ratio of the lowest LF signal magnitude to the value  $\mu$ .

During the segment proposal process, a denoised image segment with a maximum value higher than  $T_1$  is recognized as a segment with LF.

**2) Threshold Determination Stage:** This stage localizes the LF under the possible influence of residual distorted noise. The number of disjoint regions binarized by different thresholds is analyzed, and a promising threshold selection method is then proposed.

First, we describe the definition of the disjoint region of the binarized image. In this article, 8-adjacency of 1 (white pixels) is considered; the detailed explanation of adjacency can be found in [29]. A region in the binarized image is a group of adjacent pixels that can be connected to each other through the 8-adjacency path. A region can be seen as disjoint if it is not adjacent to the other regions.

Analyzing the number of disjoint regions provides the inspiration to the proposed method. The input denoised image segments are first normalized into the range of 0–1. Then, we count the

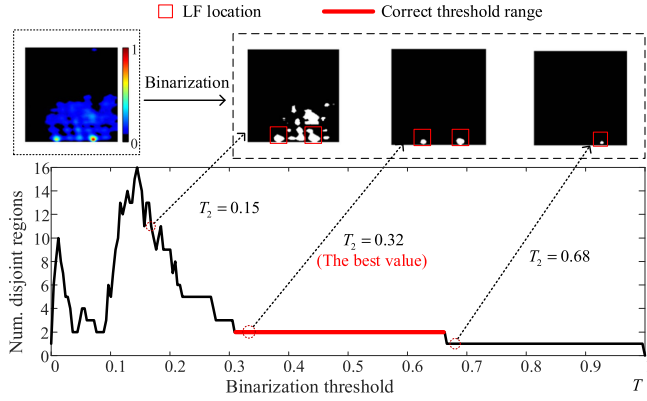


Fig. 9. Schematic of displaying LF signatures in the binarized image by considering the plateau when the number of disjoint regions changes with the binarization threshold.

numbers of disjoint regions (8-adjacency) of the input image when the input image is binarized by thresholds ranging from 0 to 1 with a step of 0.01. We use these values as the y-axis data and use the corresponding threshold as the x-axis data to draw the disjoint region number variation curve, as shown in Fig. 9. Notably, when there are only LFs shown in the binarized image, the corresponding threshold value always belongs to a “plateau.” This is because the LF signal’s grayscale value is much higher than the noise signal is. When the threshold value decreases, the LF signals are always revealed first, and it takes a rather long range of threshold descent to show another LF or noise signal. As the threshold decreases to the noise level, that is, when the threshold begins displaying noise signals, the number of disjoint regions changes quickly because the magnitude differences among different noise signals are small. Thus, even a small decrease in the binarization threshold can lead to the visualization of many new noise signals in binarized image. This phenomenon is illustrated in Fig. 9, which uses an MFL image segment with two LFs as an example. By using this principle, we can correctly find the threshold range that only shows the correct LF signature.

The detailed steps of adaptive threshold selection are as follows. At first, the normalization and disjoint regions analysis are implemented for an input image segment. Then, the numbers of disjoint regions are counted under all threshold values, as shown in the y-axis data in Fig. 9. Next, the threshold range is determined by finding a certain range of successive thresholds (plateau) that corresponds to the largest possible number of disjoint regions. The number of disjoint regions corresponding to this range is seen as the number of LF on that image segment.

**3) Binarization Stage:** This stage finally localizes LFs by using information that the first and second stage provided.

Segments without LFs are directly binarized to an all-black image. Segments with LFs use the threshold  $T_2$  determined in second stage to do binarization. In the output MFL image, the LF signatures are shown as independent white-disjoint regions. By applying this process, localizing LFs in the denoised image more accurately is possible, even for those with residual distorted noise and low-magnitude LF signals.

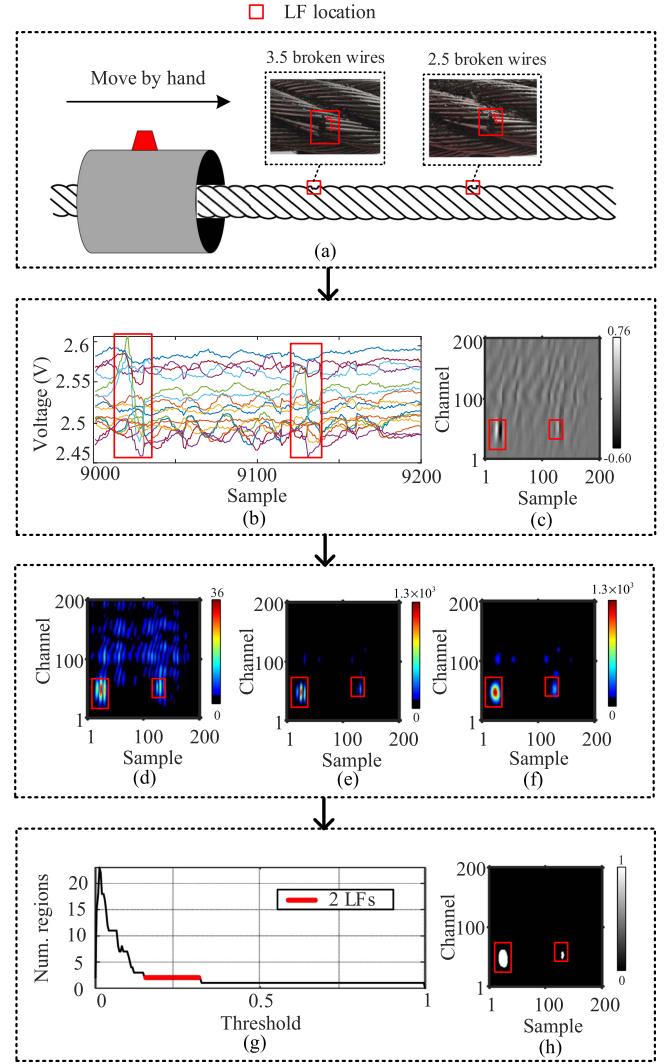


Fig. 10. Case study for the tested image. (a) Data acquisition process of an SWR with two LFs. (b) Input MFL signals. (c) Input MFL image segment. (d) MFL image segment after template matching. (e) MFL image after power law transformation. (f) MFL image after taking the envelope. (g) Disjoint region analysis for enveloped MFL image. (h) Binarized MFL image segment.

## V. CASE STUDY

After explaining the proposed method, the validation study of this method is introduced in this section. MFL inspection is implemented on an SWR with two artificial broken wire LFs. The defect condition of the LFs is shown in Fig. 10(a). An MFL signal segment with distorted noise is selected as the study subject and transferred into an MFL image segment, as shown in Fig. 10(b) and (c). The middle results of different processing stages for the tested MFL image segment are analyzed as follows.

**1) Result of Template Matching:** The method used in this step measures the similarity of image regions to the LF signal. The LF signal is extracted as high-response value regions, regardless of the noise condition, which helps the following steps to enhance further the LF. Fig. 10(d) shows that although the



response values of distorted noise are high, the template response values of the LF regions are still much higher.

**2) Result of Power Law Transformation:** Significant improvement in SNR can be seen in Fig. 10(e). In this step, the magnitudes of all regions are squared by using  $\gamma = 2$ . The amplitude differences between the distorted noise signal and the LF signal are further enlarged. SNR enhancement is realized just as verified in (5)–(7).

**3) Result of Enveloping:** The LF signatures in the previous result are transferred into single spots, as shown in Fig. 10(f). Intuitively, the LF signatures become obvious after taking the envelope. However, under the influence of residual distorted noise, the lower response magnitude LF pattern has a similar magnitude as the noise signals have. This problem poses a challenge to the localization process.

**4) Result of Adaptive Localization:** Notably, in the localization stage, even under the influence of residual noise signals in Fig. 10(f), LF signatures can still be correctly localized, as shown in Fig. 10(h). The disjoint region analysis of the enveloped image is shown in Fig. 10(g), where the threshold plateau corresponding to the two LFs is found. In contrast, the number of disjoint regions varies quickly when displaying distorted noise signals. By utilizing this feature, the proposed method precisely obtains the suitable threshold range that only shows the LF signatures.

Inspecting this MFL signal segment takes 0.27 s, which approaches a real-time response, from the user's perspective. This process is implemented on a computer with the specifications of Intel Core i7-8750H 2.20-GHz CPU with 16-GB memory using Windows 10 (64 bit). This performance can further be improved with use of high-performance hardware.

## VI. PERFORMANCE COMPARISON

To show the proposed method's superiority, performance comparison with the existing methods is conducted in this section. The denoising process and the adaptive localization process are compared with methods that have the same functions, respectively. According to existing studies, the method Ren et al. [18] proposed, which is an NFO denoising method, has the best denoising performance; thus, our denoising method is compared with this one. Regarding the localization process, we compare the proposed method with the other two existing localization methods: constant threshold binarization [18] and Canny edge detection [11]. Three MFL image segments with distorted noise are used as subjects, as shown in Fig. 11(a)–(c).

### A. Denoising Method Comparison

To measure quantitatively the performance difference of denoising methods, the SNR defined in [18, eq. (15)] is used as the performance metric. The results of three MFL images are shown in Fig. 11.

Intuitively, the resultant images that the proposed TFO method processed have much fewer obvious distorted noise signals, as shown in Fig. 11(d)–(i). In addition, as can be seen in Fig. 11(j)–(l), the SNRs of the proposed method are numerically higher than those of the NFO denoising method. Because of

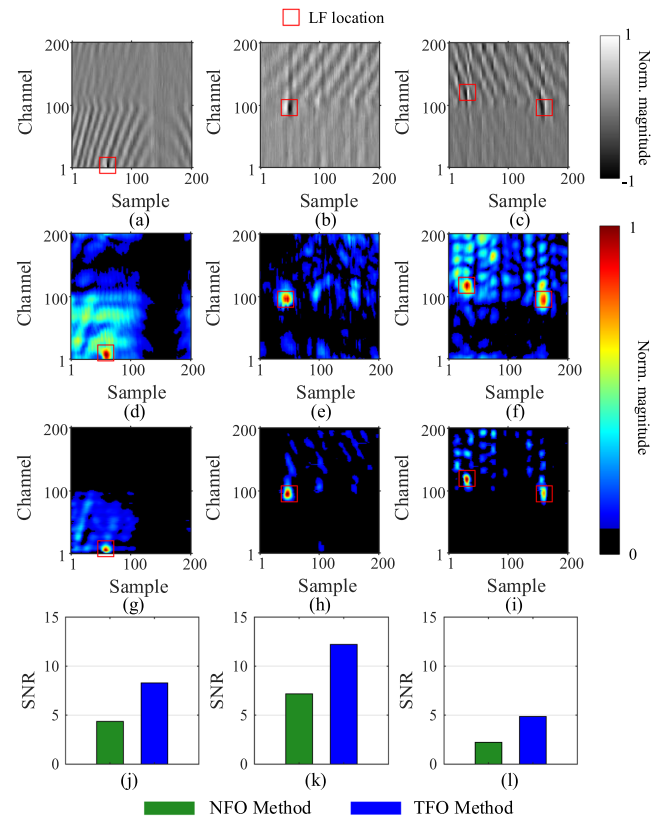


**Fig. 11.** Denoising performance comparison. (a)–(c) Input MFL image with distorted noise. (d)–(f) Denoised images processed by NFO denoising method. (g)–(i) Denoised images processed by TFO denoising method. (j)–(l) SNR comparison of NFO denoising method and TFO denoising method.

the noise distortion phenomenon, the NFO method is no longer good at removing the noise signal and it leads to a high noise magnitude after the denoising process. In contrast, the proposed TFO method can enlarge the magnitude difference between the LF signal and noise signal, regardless of the noise distortion effect, thus resulting in a much higher SNR.

### B. Localization Method Comparison

The proposed localization method is compared with the other two methods on the same dataset of denoised images. A dataset containing 1000 distorted noise MFL images is constructed as the test dataset. To compare only the performance of localization methods, the proposed denoising method first processes these images. Then, the three localization methods are implemented on these denoised images. The localization results are presented in Table I. Precision is the ratio of true positives to the sum of true positives and false positives, describing how many positives detected is the actual positive. Recall is the ratio of true positives to the sum of true positives and false negatives, describing how many actual positives are successfully detected. The F1 score is defined as the harmonic mean of the precision and recall.

An independent 8-adjacency disjoint region is regarded as a positive detection in the binarized result. The F1 score is used as the comprehensive performance metric because it balances



TABLE I  
LOCALIZATION PERFORMANCE COMPARISON

Performance metrics	Constant threshold binarization [18]	Canny edge detection [11]	The proposed method
Number of true positives	715	770	729
Number of false positives	1677	54 053	118
Number of false negatives	55	0	41
Precision	29.89%	1.40%	<b>86.07%</b>
Recall	92.86%	100%	<b>94.68%</b>
F1 score	0.4522	0.0277	<b>0.9017</b>

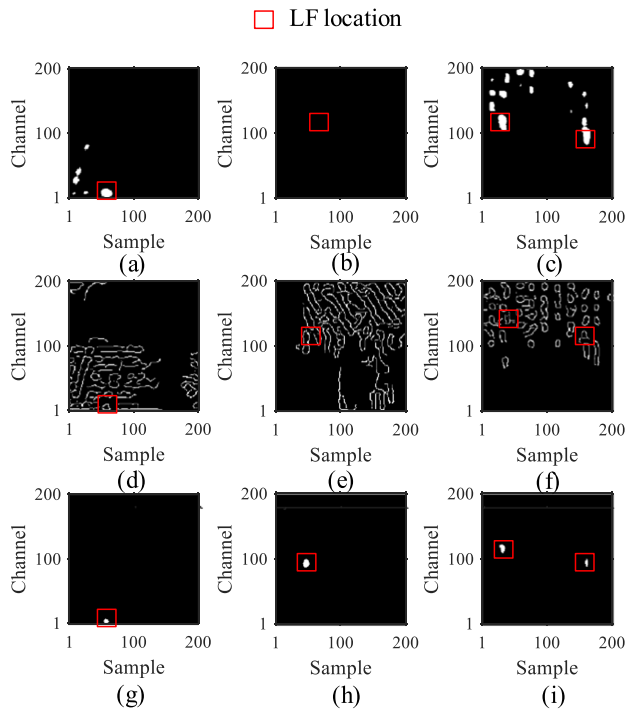


Fig. 12. Localization performance comparison. (a)–(c) Localization results from the constant threshold method. (d)–(f) Localization results of the Canny edge detection method. (g)–(i) Localization results of the proposed disjoint region analysis-based method.

the result of both the precision and the recall rate. Based on this, the proposed localization method remarkably improves the performance of the localization methods. The F1 score of the proposed method is 0.9017, which is much higher than those of constant threshold method (0.4522) and Canny edge detection method (0.0277).

To illustrate more intuitively the performance difference of the localization methods, three denoised images processed by the proposed method in Fig. 11 are used as examples. The localization results shown in Fig. 12 can provide sufficient explanations for the results in Table I.

The constant threshold method needs the manual setting of a tradeoff threshold value. This method can cause miss detection, as shown in Fig. 12(b), and false positives, as shown in Fig. 12(a) and (c). The Canny edge detection method is too sensitive to the magnitude variation. Although all LFs can be detected, too many false positives make LF identification very difficult, as

shown in Fig. 12(d)–(f). The proposed method can automatically obtain the suitable threshold and has a high resistance to residual noise patterns, thus providing accurate results, as shown in Fig. 12(g)–(i).

## VII. CONCLUSION

In this article, the noise distortion phenomenon was studied, and a fault diagnosis method combined with LF enhancement and adaptive localization was proposed to detect LFs under a noise distortion condition. The influence of noise distortion on the noise signal and LF signal was first analyzed. We found that the noise features were vulnerable to noise distortion while LF features remained stable, regardless of the noise condition. Therefore, a TFO denoising method was proposed to improve the SNR under the noise distortion phenomenon. In addition, as the denoised results of MFL images with distorted noise were still inevitably influenced by residual distorted noise signals, a three-stage adaptive localization method based on disjoint region analysis was proposed to localize automatically the LFs in the denoised images. From the experimental results, the proposed TFO denoising method could produce higher SNR results (nearly doubled) than the state-of-the-art denoising method. The proposed localization method significantly reduced the number of false positives and had a better F1 score (0.9017) than those of the existing methods (0.4522 for constant threshold method and 0.0277 for Canny detection method).

## REFERENCES

- [1] P. Zhou, G. Zhou, Z. Zhu, Z. He, X. Ding, and C. Tang, "A review of non-destructive damage detection methods for steel wire ropes," *Appl. Sci.*, vol. 9, no. 13, 2019, Art. no. 2771, doi: [10.3390/app9132771](https://doi.org/10.3390/app9132771).
- [2] S. Liu, Y. Sun, X. Jiang, and Y. Kang, "A review of wire rope detection methods, sensors and signal processing techniques," *J. Nondestruct. Eval.*, vol. 39, no. 4, pp. 1–18, 2020, doi: [10.1007/s10921-020-00732-y](https://doi.org/10.1007/s10921-020-00732-y).
- [3] H. Mouradi, A. El Barkany, and A. Biyaali, "Investigation on the main degradation mechanisms of steel wire ropes: A literature review," *J. Eng. Appl. Sci.*, vol. 11, pp. 1206–1217, 2016, doi: [10.3923/jeasci.2016.1206.1217](https://doi.org/10.3923/jeasci.2016.1206.1217).
- [4] P. Zhou, G. Zhou, H. Wang, D. Wang, and Z. He, "Automatic detection of industrial wire rope surface damage using deep learning-based visual perception technology," *IEEE Trans. Instrum. Meas.*, vol. 70, 2021, Art. no. 5002911, doi: [10.1109/TIM.2020.3011762](https://doi.org/10.1109/TIM.2020.3011762).
- [5] P. Zhou, G. Zhou, Y. Li, Z. He, and Y. Liu, "A hybrid data-driven method for wire rope surface defect detection," *IEEE Sensors J.*, vol. 20, no. 15, pp. 8297–8306, Aug. 2020, doi: [10.1109/jsen.2020.2970070](https://doi.org/10.1109/jsen.2020.2970070).
- [6] P. Zhou, G. Zhou, Z. He, C. Tang, Z. Zhu, and W. Li, "A novel texture-based damage detection method for wire ropes," *Measurement*, vol. 148, 2019, Art. no. 106954, doi: [10.1016/j.measurement.2019.106954](https://doi.org/10.1016/j.measurement.2019.106954).
- [7] J. Zhang and S. Wang, "Nondestructive testing of wire ropes based on image fusion of leakage flux and visible light," *J. Failure Anal. Prevention*, vol. 19, no. 2, pp. 551–560, 2019, doi: [10.1007/s11668-019-00634-w](https://doi.org/10.1007/s11668-019-00634-w).
- [8] F. Pan, L. Ren, J. Zhou, and Z. Liu, "Fault classification based on computer vision for steel wire ropes," *J. Phys., Conf. Ser.*, vol. 2184, no. 1, 2022, Art. no. 012035, doi: [10.1088/1742-6596/2184/1/012035](https://doi.org/10.1088/1742-6596/2184/1/012035).
- [9] E.-S. Platzer, J. Nägele, K.-H. Wehking, and J. Denzler, "Hmm-based defect localization in wire ropes—A new approach to unusual subsequence recognition," in *Proc. Joint Pattern Recognit. Symp.*, 2009, pp. 442–451.
- [10] R. Raišutis, R. Kažys, L. Mažeika, E. Žukauskas, V. Samaitis, and A. Jankauskas, "Ultrasonic guided wave-based testing technique for inspection of multi-wire rope structures," *Nephrol. Dialysis Transplant. E Int.*, vol. 62, pp. 40–49, 2014, doi: [10.1016/j.ndteint.2013.11.005](https://doi.org/10.1016/j.ndteint.2013.11.005).
- [11] X. Tan and J. Zhang, "Evaluation of composite wire ropes using unsaturated magnetic excitation and reconstruction image with super-resolution," *Appl. Sci.*, vol. 8, no. 5, 2018, Art. no. 767, doi: [10.3390/app8050767](https://doi.org/10.3390/app8050767).

- [12] J. Zhang, S. Lu, and T. Gao, "Quantitative detection of remanence in broken wire rope based on adaptive filtering and Elman neural network," *J. Failure Anal. Prevention*, vol. 19, no. 5, pp. 1264–1274, 2019, doi: [10.1007/s11668-019-00709-8](#).
- [13] J.-W. Kim and S. Park, "Magnetic flux leakage sensing and artificial neural network pattern recognition-based automated damage detection and quantification for wire rope non-destructive evaluation," *Sensors*, vol. 18, no. 1, 2018, Art. no. 109, doi: [10.3390/s18010109](#).
- [14] C. Jomdech and A. Prateepasen, "Design of modified electromagnetic main-flux for steel wire rope inspection," *Nephrol. Dialysis Transplant. E Int.*, vol. 42, no. 1, pp. 77–83, 2009, doi: [10.1016/j.ndteint.2007.10.006](#).
- [15] S. Park, J.-W. Kim, C. Lee, and J.-J. Lee, "Magnetic flux leakage sensing-based steel cable NDE technique," *Shock Vib.*, vol. 2014, 2014, Art. no. 929341, doi: [10.1155/2014/929341](#).
- [16] D. Mukherjee, S. Saha, and S. Mukhopadhyay, "An adaptive channel equalization algorithm for MFL signal," *Nephrol. Dialysis Transplant. E Int.*, vol. 45, no. 1, pp. 111–119, 2012, doi: [10.1016/j.ndteint.2011.08.011](#).
- [17] Z. Zhou and Z. Liu, "Fault diagnosis of steel wire ropes based on magnetic flux leakage imaging under strong shaking and strand noises," *IEEE Trans. Ind. Electron.*, vol. 68, no. 3, pp. 2543–2553, Mar. 2021, doi: [10.1109/TIE.2020.2973874](#).
- [18] L. Ren, Z. Liu, and J. Zhou, "Shaking noise elimination for detecting local flaw in steel wire ropes based on magnetic flux leakage detection," *IEEE Trans. Instrum. Meas.*, vol. 70, 2021, Art. no. 3524909, doi: [10.1109/tim.2021.3112792](#).
- [19] J. Zhang, X. Tan, and P. Zheng, "Non-destructive detection of wire rope discontinuities from residual magnetic field images using the Hilbert-Huang transform and compressed sensing," *Sensors*, vol. 17, no. 3, 2017, Art. no. 608, doi: [10.3390/s17030608](#).
- [20] Z. Liu et al., "Improved Hilbert–Huang transform with soft sifting stopping criterion and its application to fault diagnosis of wheelset bearings," *Int. Soc. Automat. Trans.*, vol. 125, pp. 426–444, 2022, doi: [10.1016/j.isatra.2021.07.011](#).
- [21] Z. Liu and L. Ren, "Shaking noise exploration and elimination for detecting local flaws of steel wire ropes based on magnetic flux leakages," *IEEE Trans. Ind. Electron.*, vol. 70, no. 4, pp. 4206–4216, Apr. 2023, doi: [10.1109/TIE.2022.3174302](#).
- [22] S. Liu et al., "A new signal processing method based on notch filtering and wavelet denoising in wire rope inspection," *J. Nondestruct. Eval.*, vol. 38, no. 2, pp. 1–14, 2019, doi: [10.1007/s10921-019-0580-y](#).
- [23] D. Zhang, M. Zhao, Z. Zhou, and S. Pan, "Characterization of wire rope defects with gray level co-occurrence matrix of magnetic flux leakage images," *J. Nondestruct. Eval.*, vol. 32, no. 1, pp. 37–43, 2012, doi: [10.1007/s10921-012-0156-6](#).
- [24] L. Yang, X. Wu, D. Zhao, H. Li, and J. Zhai, "An improved Prewitt algorithm for edge detection based on noised image," in *Proc. 4th Int. Congr. Image Signal Process.*, 2011, vol. 3, pp. 1197–1200.
- [25] C.-M. Tsai, "Adaptive local power-law transformation for color image enhancement," *Appl. Math. Inf. Sci.*, vol. 7, no. 5, pp. 2019–2026, 2013, doi: [10.12785/amis/070542](#).
- [26] K. Wang, "A study of cubic spline interpolation," *InSight, Rivier Acad. J.*, vol. 9, no. 2, pp. 1–15, 2013.
- [27] R. Girshick, J. Donahue, T. Darrell, and J. Malik, "Rich feature hierarchies for accurate object detection and semantic segmentation," presented at the IEEE Conf. Comput. Vis. Pattern Recognit., 2014, pp. 580–587, doi: [10.1109/CVPR.2014.81](#).
- [28] H. Rohling, "Radar CFAR thresholding in clutter and multiple target situations," *IEEE Trans. Aerosp. Electron. Syst.*, vol. AES-19, no. 4, pp. 608–621, Jul. 1983, doi: [10.1109/TAES.1983.309350](#).
- [29] R. C. Gonzalez and R. E. Woods, *Digital Image Processing*, 4th ed. London, U.K.: Pearson Education, 2017, ch. 2, pp. 79–83.



**Feiyang Pan** was born in Danjiangkou, Hubei, China. He received the B.Eng. degree in electronic information engineering from the University of Electronic Science and Technology of China, Chengdu, China, and the Eng. (Hons.) degree in electrical and electronics engineering from the University of Glasgow, Glasgow, U.K., in 2022. He is currently working toward the M.Sc. degree in precision machine and precision instrument with the University of Science and Technology of China, Hefei, China.

His research interests include nondestructive tests, biomedical optics, and biomedical image processing



**Zhiliang Liu** (Member, IEEE) was born in Rizhao, Shandong, China, in 1984. He received the Ph.D. degree from the School of Automation Engineering, University of Electronic Science and Technology of China (UESTC), Chengdu, China, in 2013.

From 2009 to 2011, he was with the University of Alberta as a visiting scholar. From 2013 to 2015, he was an Assistant Professor with UESTC's School of Mechanical and Electrical Engineering, where since 2015, he has been an Associate Professor with the same department. He has authored or coauthored more than 100 papers, including 40+ SCI-indexed journal papers. He currently holds 18 research grants from the National Natural Science Foundation of China, Open Grants of National Key Laboratory, and China Postdoctoral Science Foundation, among others. His research interests include fault diagnosis and prognostics of rotating machinery by using advanced signal processing and data-mining methods.



**Liyuan Ren** was born in Xichang, Sichuan, China. He received the B.Eng. degree in electronic information engineering from the University of Electronic Science and Technology of China, Chengdu, China, in 2020, and the Eng. (Hons.) degree in electrical and electronics engineering from the University of Glasgow, Glasgow, U.K., in 2020. He is currently working toward the M.Sc. degree in signal and systems with the Delft University of Technology (TU Delft), Delft, The Netherlands.

His research interests include nondestructive tests, automotive radar, and multisensor navigation.



**Mingjian Zuo** (Senior Member, IEEE) received the B.Sc. degree in agricultural engineering from the Shandong Institute of Technology, Shandong, China, in 1982 and the M.Sc. and Ph.D. degrees in industrial engineering from Iowa State University, Ames, IA, USA, in 1986 and 1989, respectively.

He is a Principal Scientist with Qingdao International Academician Park Research Institute, Qingdao, China, and a Guest Professor with the University of Electronic Science and Technology of China, Chengdu, China. He served as the Department Editor for *IJSE Transactions*, an Associate Editor for *IEEE TRANSACTIONS ON RELIABILITY*, *Journal of Risk and Reliability*, *International Journal of Quality, Reliability and Safety Engineering*, a Regional Editor for *International Journal of Strategic Engineering Asset Management*, and was an editorial board member for *Reliability Engineering and System Safety*, *Journal of Traffic and Transportation Engineering*, and *International Journal of Performance Engineering*. His research interests include system reliability analysis, maintenance modeling and optimization, signal processing, and fault diagnosis.

Dr. Zuo is a Fellow of the Canadian Academy of Engineering, the Institute of Industrial and Systems Engineers, the Engineering Institute of Canada, and a Founding Fellow of the International Society of Engineering Asset Management.